Journal of Pharmaceutical Sciences 109 (2020) 452-463

Contents lists available at ScienceDirect

Journal of Pharmaceutical Sciences

journal homepage: www.jpharmsci.org

Pharmaceutical Biotechnology

Evaluation of Nanoparticle Tracking Analysis for the Detection of Rod-Shaped Particles and Protein Aggregates

Brandon M. Hoover [1], Regina M. Murphy [2,*]

[1] Biophysics Program, University of Wisconsin, Madison, Wisconsin 53706
[2] Department of Chemical and Biological Engineering, University of Wisconsin, Madison, Wisconsin 53706

ARTICLE INFO

Article history:
Received 18 June 2019
Revised 30 September 2019
Accepted 3 October 2019
Available online 8 October 2019

Keywords:
Alzheimer's disease
nanoparticle analysis
protein aggregation
light scattering
particle size
nanotechnology
kinetics

ABSTRACT

Nanoparticle tracking analysis (NTA) is an important technique for measuring hydrodynamic size of globular biological particles including liposomes and viruses. Less attention has been paid to NTA of rod-like particles, despite their considerable interest. For example, amyloid fibrils and protofibrils are protein aggregates with rod-like morphology, diameters of 2-15 nm, and lengths from 50 nm to 1 μm, and linked to diseases including Alzheimer's and Parkinson's. We used NTA to measure the concentration and hydrodynamic size of gold nanorods (10 nm diameter, 35-250 nm length) and myosin (2 nm diameter, 160 nm length), as models of rod-like particles. Measured hydrodynamic diameters of gold nanorods were consistent with theoretical calculations, as long as particle concentration and solution conditions were controlled. Myosin monomers were invisible by NTA, but a small population of aggregates was detected. We combined NTA results with other light scattering data to gain insight into number and size distribution of protein solutions containing both monomer and aggregates. Finally, we demonstrated the utility of NTA and its limitations by characterizing aggregates of alpha-synuclein. Of note is the use of NTA to detect a change in morphology from compact to elongated by analyzing the ratio of hydrodynamic size to intensity.

Introduction

Deposition of amyloid fibrils in tissues is linked to several neurodegenerative disorders including Alzheimer's, Parkinson's, and Huntington's disease. Although the proteins associated with each disease are distinctly different (e.g., β-amyloid in Alzheimer's disease, α-synuclein in Parkinson's disease), the aggregates (fibrils and protofibrils) share a common cross-β sheet structure and an anisotropic rod-like shape, with typical cross-sectional diameters of 2-15 nm and lengths of 50 nm-1 μm. On account of the importance of amyloid fibril formation in neurodegenerative diseases, many research groups have probed the kinetics of formation and used experimental data to build kinetic models and infer a mechanism.[1-8] Mechanistic-based kinetic models can be reliably determined only if both aggregate molar (number) concentration and aggregate size distribution are measured.[9] Most desirable are methods that are non-invasive and non-destructive, that are amenable to a variety of solution conditions, and that do not require labeling. Thioflavin T (ThT) fluorescence is perhaps the most commonly chosen experimental technique for detecting amyloid, reporting on the relative mass concentration of fibrillar aggregates. However, ThT provides no information about fibril number concentration or fibril size.

In processing and formulation of protein pharmaceuticals, the unwanted formation of aggregates is a critical concern; aggregates can affect efficacy and can be immunogenic. Here, too, the ability to rapidly detect and quantify protein aggregates is important. Aggregate hydrodynamic size can be measured in solution using dynamic light scattering (DLS). No labeling is required, and measurements are rapid.[10] However, DLS cannot measure the number concentration of aggregates, and only averaged properties are obtained. Other tools such as transmission electron microscopy (TEM) and atomic force microscopy are invaluable in providing detailed information on aggregate dimensions and morphological and mechanical characteristics,[11] but quantitation of the entire population

Abbreviations used: aSyn, alpha-synuclein; CTAB, cetrimonium bromide; d_h, hydrodynamic diameter; DI, deionized; DLS, dynamic light scattering; *M*, molecular weight; NTA, nanoparticle tracking analysis; N_p, particle number concentration; TEM, transmission electron microscopy; ThT, thioflavin-T; SLS, static light scattering.

This article contains supplementary material available from the authors by request or via the Internet at https://doi.org/10.1016/j.xphs.2019.10.006.

* *Correspondence to:* Regina M. Murphy (Telephone: +1-6082621587).
E-mail address: regina.murphy@wisc.edu (R.M. Murphy).

https://doi.org/10.1016/j.xphs.2019.10.006
0022-3549/

is challenging. Size exclusion chromatography is useful for measuring the rate of monomer loss, but the method is insensitive to small quantities of aggregates.[12] Fluorescence correlation spectroscopy and related techniques provide rapid analysis and can yield size information[13,14] but usually require chemical labeling.

Nanoparticle tracking (NTA) is a scattering technique that tracks the diffusion of individual particles in solution and, uniquely distinct from DLS, can report on particle number concentration, mean hydrodynamic size, and particle-by-particle size distribution.[15] NTA has become an important tool for characterizing biological materials with spherical or globular morphology such as liposomes and protein aggregates.[16-22] However, less is known about its use for anisotropic particles. In previous work, we used DNA (12.3 kb, 4100 nm long) as a model for elongated chain-like particles.[15] While the measured hydrodynamic size obtained by NTA was accurate, the measured particle number concentration was too low by 1000×, even with a high-sensitivity camera. We also collected NTA data on the kinetics of aggregation of the Alzheimer-related peptide, β-amyloid, and again observed a discrepancy between the expected and measured number of particles.

In work reported here, we conducted a more detailed evaluation of the potential of NTA for experimental characterization of rod-like particles and protein aggregates. We first tested the technique on gold nanorods with dimensions similar to smaller amyloid fibrils or protofibrils. The nanorods have a narrow size distribution and provide an excellent model system for evaluation of the reliability of NTA at obtaining quantitative size and concentration data of rod-like particles. We next used NTA, supplemented with DLS and TEM, to characterize a solution of myosin, which was chosen because its rod-like nature, rigidity, and length (160 nm) made it an attractive protein model of smaller protofibrils. Finally, we evaluated the ability of NTA to track aggregation of the fibril-forming protein, α-synuclein. With NTA, hydrodynamic size and scattering intensity are simultaneously tracked on a particle-by-particle basis, and we demonstrate how these data can be evaluated to detect a shift in particle morphology. Our results point to both the promise and the limitations of NTA and show that more comprehensive results are obtained, when results from NTA are interpreted in combination with data obtained using other light scattering techniques.

Experimental Procedures

Nanoparticle Tracking Analysis

All NTA measurements were performed with a Nanosight LM10 (Nanosight, Salisbury, UK) equipped with a high-sensitivity electron-multiplying charge-coupled device camera and a 485 nm laser. Briefly, particles in the sample scatter light from an incident laser, and the scattered light is tracked using a high-sensitivity camera. By measuring the trajectory of the diffusing particle over a tracking time t, the diffusion coefficient D_t and hydrodynamic diameter d_h are obtained.[16,17] The number of scattering particles in the sample chamber is tracked and converted to a particle number concentration N_p. Video tracking was acquired for 30 s time intervals with at least 3 measurements for each sample. Analysis of the particle concentration, mean size, and standard deviation of particle tracks was conducted using NTA 3.0 software.

Gold Nanorods

Gold nanorods with cross-sectional diameter of 10 nm and lengths 35 nm (A12-10-750-CTAB-25), 100 nm (A12-10-2100-CTAB-DIH-5), and 250 nm (A12-10-1400-5-CTAB-DIH), all coated with centrimonium bromide (CTAB), or length of 100 nm coated with NanoPartz positive polymer (A12-10-1400-5-POS-DIH), were purchased from NanoPartz Inc (Loveland, CO). While the gold nanorod diameter is 10 nm, the CTAB bilayer has been estimated to be 3.9 nm thick,[23] so the diameter of the CTAB-coated rods was taken to be 17.8 nm. The polymer coating was reported by the manufacturer to add 1.5 nm in diameter, giving an overall rod diameter of 11.5 nm.

Before use, rods were bath sonicated for 15 min at room temperature. Ultrapure 0.5 mM CTAB (NanoPartz) was dissolved in deionized (DI) water and then step filtered together through 0.45-μm, 0.22-μm, and 0.02-μm filters (Millipore, Burlington, MA), after which nanorods were diluted into filtered CTAB solutions. To mitigate particle shedding, the first 3 drops were discarded following each filtration step. For NTA particle quantification, samples were prepared at expected concentrations of 5×10^7, 5×10^8, and 5×10^9 particles/mL, based on the manufacturer's reported stock concentrations. Camera levels of 13, 10, and 7 were used for the 35 nm, 100 nm, and 250 nm rods, respectively, with a detection threshold of 5.

To produce polydisperse samples, 35 nm and 250 nm rods were mixed at number ratios of 1:1 and 10:1 (35 nm:250 nm) in step filtered 0.5 mM CTAB solutions for a total particle concentration of 4×10^9 particles/mL. For the 1:1 and 10:1 sample, a camera level of 7 and 13, respectively, was used, with a detection threshold of 5.

Myosin

Myosin (calcium activated from rabbit skeletal muscle, Sigma M1636) was diluted to 0.5 mg/mL in 0.6 M KCl, 5 mM KH_2PO_4, 5 mM K_2HPO_4, 5 mM $MgCl_2$, 1 mM ethylene glycol bis(2-aminomethyl) tetraacetic acid, 1 mM dithiothreitol, and 1 mM MgATP, pH 7.4. The sample was centrifuged at 100,000× g for 45 min at 4°C and the pellet discarded. Protein concentration was determined by using an extinction coefficient[24] of $\varepsilon_{280}^{1\%} = 5.0$.

Myosin prepared for NTA was serially diluted by factors of 10 into 0.02-μm filtered buffer and injected into the sample chamber using a 0.45-μm filter. A camera level of 13 and detection threshold of 5 was used for each sample.

Myosin samples were further characterized by static light scattering (SLS) and DLS and by TEM. For SLS and DLS, myosin was filtered through a 0.45-μm filter directly into a precleaned quartz cuvette, placed in a temperature-controlled bath containing the index matching fluid decahydronaphthalene (Sigma, St. Louis, MO) equilibrated at 24°C. Data were obtained using a Brookhaven BI-200SM system (Brookhaven Instruments, Holtsville, NY) and an Innova 90C argon laser operated at 488 nm (Coherent, Inc., Santa Carla, CA). DLS measurements were collected for 5 min at a 90° scattering angle. Autocorrelation functions were analyzed using the method of cumulants to determine a z-average hydrodynamic diameter and using CONTIN to obtain an intensity-weighted size distribution as previously described.[25] For SLS, scattered intensity from myosin solution was collected at detector angles of 40°-120°. The raw scattering intensity of the background buffer and a toluene standard were also recorded. The Rayleigh ratio $R(q)$ was determined as described previously,[10] and the data were fit to the Zimm equation:

$$\frac{Kc}{R(q)} = \frac{1}{M_w}\left(1 + \frac{q^2 R_g^2}{3}\right) + 2B_2 c \tag{1}$$

where M_w is the weight-average molecular weight, R_g is the radius of gyration, c is the mass concentration (g/cm^3), B_2 is the second virial coefficient (mol-cm^3/g^2), $K = 4\pi^2 n_S^2 (dn/dc)^2 / N_A \lambda^4$, $q = 4\pi n_S \sin(\theta/2)/\lambda$, n_S, N_A, λ, and θ are the refractive index of the solvent, Avogadro's number, laser wavelength, and scattering angle, respectively, and dn/dc is the refractive index increment and taken

to be 0.186 cm^3/g. B_2 was calculated from the excluded volume for rods of length L and diameter d as

$$B_2 = \frac{2\pi N_A \pi}{M_W^2 4} L^2 d.$$

To obtain TEM images, myosin was fixed on a pioloform-coated grid and stained with a solution containing 2% methylamine tungstate. Approximately, 5 μL of sample was placed on the grid and washed with myosin buffer. Excess buffer was removed by contact with filter paper. A solution containing 2% methylamine tungstate was then applied to the grid. Following ~10 s, excess stain was removed using filter paper. The grid was dried for several hours at room temperature. Images were acquired with a Philips CM120 scanning transmission electron microscope (FEI Corp, Hillsboro, OR). A total of 13 globular aggregates were tracked across 7 images.

IgM

IgM from human serum (Sigma, I8260) was used without further purification. Samples were prepared in a 0.02-μm filtered solution of 0.05 M Tris-HCl, 0.2 M NaCl, 15 mM NaN_3, pH 8.0. IgM concentration was determined using an extinction coefficient[26] of $\epsilon_{280}^{0.1\%} = 1.18$. For NTA measurements, a camera level of 13, and detection threshold of 5 was used.

Alpha-Synuclein

The human a*lpha-synuclein* (aSyn) gene was ligated into the pTXB1 plasmid (NE Biolabs, Ipswitch, MA) using the Nde I and Spe I restriction sites and transformed into BL21-DE3 cells (NE Biolabs). Cells were cultured in 100 mg/mL ampicillin, and protein expression was induced with 0.5 mM isopropyl-β-D-thiogalactoside. Cells were lysed by sonication, and the crude lysate was applied to a chitin affinity column (NE Biolabs). The column was washed extensively to remove non-specifically bound material, first with column buffer (20 mM Tris-HCl, 500 mM NaCl, 1 mM EDTA, pH 9.0) containing 2 M urea and then with column buffer without urea. The target protein was cleaved from the chitin-binding tag overnight at room temperature by equilibration with 75 mM dithiothreitol in column buffer. The protein was eluted and dialyzed extensively against phosphate-buffered saline (PBS: 10 mM KH_2PO_4/K_2HPO_4 100 mM NaCl, pH 7.4). The protein was concentrated by centrifugal ultrafiltration in a 3 kDa membrane (Amicon Ultra-15) to ~400 μM determined by absorbance spectroscopy using a molar extinction coefficient[3] of 5600 M^{-1} at 275 nm. aSyn was then boiled for 15 min to remove remaining impurities and centrifuged at 10,000× *g* for 10 min, and the supernatant was collected. Protein samples were aliquoted, flash frozen, and stored at −80°C.

To prepare aggregated samples, stock aSyn solutions were thawed and then diluted into PBS to 100 μM final concentration. The sample was subjected to continuous shaking using an Ambion vortex adapter-60 (Thermofisher, Waltham, MA) connected to a vortexer (Thermofisher) at a vortex level of 3 for 48 h at 37°C. The intensity of shaking was quantified by measuring the 3D vibrational acceleration over 1 min using the VibSensor app on an iPhone XS (Apple, Cupertino, CA). Vibrational peak accelerations in x, y, and z were measured at 52.3, 38.5, and 51 m/s^2, respectively (Supporting Information Fig. 1).

aSyn fibril formation was monitored by ThT (Sigma) fluorescence measured at 0 h, 24 h, and 48 h after initiation of mechanical agitation. Briefly, samples were prepared with 2 μM protein and 10 μM ThT. Fluorescence emission was measured at an excitation of 440 nm and emission at 485 nm using a QuantaMaster spectrofluorimeter (PTI, Birmingham, NJ). Three spectra for each sample were taken and averaged, and the background fluorescence of ThT in buffer alone at 485 nm was subtracted.

aSyn aliquots were taken at 0 h, 24 h and 48 h after initiation of mechanical agitation and characterized by NTA and TEM. For NTA, samples were diluted into 0.02-μm prefiltered PBS. At 0 h, aSyn was diluted to 10 μM, and at 24 and 48 h, dilution was adjusted to reach a desired particle number concentration near 10^9 particles/mL. For the 48 h sample, measurements were taken both before and after centrifugation (4000 RPM for 20 min at room temperature using an Eppendorf 5804R) (Hamburg, Germany). For all NTA samples at each time point, a camera level of 13, and detection threshold of 5 was used. Negative stain images of aSyn were acquired with a Tecnai T12 TEM (FEI Corp, Hillsboro, OR) using 1% uranyl acetate. In addition, aSyn was diluted by a factor of 30 at 48 h, centrifuged, and characterized by DLS, as described for myosin.

Results and Discussion

Gold Nanorods as Models of Rod-Like Particles

NTA does not require calibration, but to have confidence in the accuracy, reliability, and reproducibility of measurements, standards are needed for validation. For spheres, polystyrene latex beads are available as monodisperse particles of defined diameter. NTA size measurements are accurate with these particles; for example, we measured diameters of 59 ± 3 nm for 60 nm beads and 239 ± 5 nm for 240 nm beads.[15] However, validation of the technique with defined-size rod-like particles has not, to our knowledge, been reported previously. To evaluate NTA as a tool for measuring size and number concentration of submicron-sized rod-like particles, we chose to test commercially available gold nanorods with lengths of 35 nm, 100 nm, and 250 nm. The properties of gold nanorods have been characterized by others using DLS.[27] To convert nanorod dimensions to NTA size measurements, the theoretical values of translational diffusion D_t and hydrodynamic diameter d_h of rod-like particles were calculated according to Tirado and Garcia de la Torre[28]:

$$D_t = \frac{k_B T}{3\pi\eta L}\left[\ln\left(\frac{L}{d}\right) + \nu\right] \tag{2}$$

$$\upsilon = 0.312 + 0.565\frac{d}{L} - 0.1\frac{d^2}{L^2}$$

and the Stokes-Einstein relationship:

$$d_h = \frac{k_B T}{3\pi\eta D_t}. \tag{3}$$

where k_B is the Boltzmann constant, T is the temperature, η is the viscosity of water, L is the rod length, and d is the cross-sectional diameter of rods.

Because bare gold nanorods tend to aggregate in aqueous solutions, we tested bare nanorods in water and in CTAB-containing solutions as well as nanorods coated with NanoPartz Positive Polymer. First, we evaluated the effect of surfactant on nanorod dispersion by using NTA to characterize 100 nm-long gold nanorods in DI water or 0.5 mM CTAB. A representative comparison of the size distribution is shown in Figure 1a. The theoretical d_h for rods of this dimension is 49 nm (Eqs. 2 and 3), a close match to the measured value in CTAB. In contrast, the measured size in water was about 50% larger, whereas the total measured number of particles in water was about one-third that in CTAB. This indicates that the rods are aggregated when diluted into water whereas they remain mostly dispersed when added to CTAB-containing water

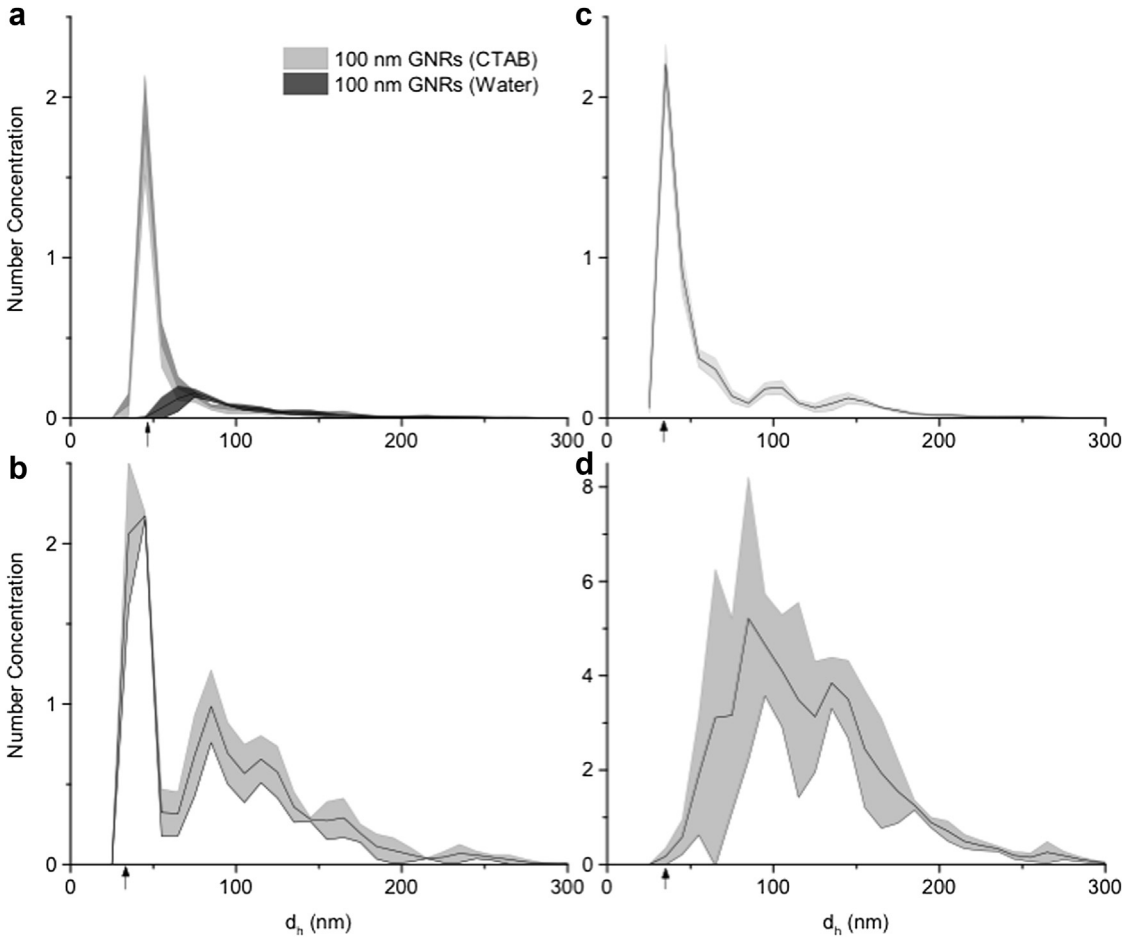

Figure 1. (a) Particle size distribution of 100 nm gold nanorods (GNRs) diluted into 0.5 mM CTAB (light gray) and water (dark gray). (b-d) 35 nm GNRs were diluted into 0.5 mM CTAB with a calculated rod concentration of 5×10^9 (b), 5×10^8 (c), and 5×10^7 (d) particles/mL. Background scattering of CTAB increases with rod dilution. Number concentration is per 10^9 (a), 10^9 (b), 10^8 (c), and 10^7 (d) particles/mL respectively. Shading represents the standard deviation of 3 independent replicates. Arrows indicate the theoretical value of d_h.

and demonstrates that NTA can sensitively measure solvent effects on aggregation. A comparison of theory with measurements can shed light on whether the nanorod aggregates in water are bundled side-by-side or elongated end-to-end. Based on the ratio of the particle number concentration N_p in water versus in CTAB solution, we estimated that the average aggregate in water contains 3 nanorods. If aggregation is head-to-tail (300 nm long, 17.8 nm diameter), the theoretical $d_h = 95$ nm, whereas if bundled side-by-side, the theoretical $d_h = 62$ nm. A comparison with the size distribution shown in Figure 1a indicates that the aggregate size is consistent with side-by-side rather than head-to-tail aggregates.

In a control experiment, we found that in 0.02 μm-filtered 0.5 mM CTAB in DI water, a high concentration of background aggregates was detected (~5×10^8 particles/mL with mean d_h ~ 118 nm, Supporting Information Fig. 2). The first few drops were discarded to mitigate contaminants due to particle shedding. By the same procedure, no particles were observed in pure DI water (data not shown). These aggregates are too large to be CTAB micelles.[29-31] Rather, the particles are likely contaminants complexed with the detergent. Thus, although CTAB is necessary for dispersion of gold nanorods, contributions from buffer contaminants must be considered in NTA data analysis.

We next evaluated 35 nm-long nanorods in 0.5 mM CTAB, at 3 dilutions. Representative size distributions are shown in Figures 1b-1d, and data are summarized in Table 1. At the highest concentration, the measured N_p was equal to that expected, and the peak in the size distribution corresponded closely to the theoretical d_h (Fig. 1b, Table 1). A 10-fold dilution yielded a N_p higher than expected (Table 1). The major peak in the size distribution was correct, but a second population of larger (~100 nm) particles was evident (Fig. 1c). This second population can be ascribed to the contaminants from the CTAB solution. With a further 10-fold dilution, the nanorods were undetectable, and background buffer was the dominant contributor (Fig. 1d, Table 1).

Experiments were repeated with CTAB-coated nanorods (in 0.5 mM CTAB) of 100 or 250 nm length. Results are summarized in Table 1. At the highest concentration tested, the mode of the size distribution was very close to the theoretical d_h. The mean was larger than the mode and showed greater variability with dilution; this effect was less for the larger 250 nm rods than for the smaller rods. We attribute this outcome to background contributions becoming less significant as the scattering contribution from the larger nanorods increases, masking weakly scattering background contaminants from detection. For 100 nm-long CTAB-coated rods, the mismatch between measured and expected N_p is extremely large, which we attribute to an error in the manufacturer's reported concentration. With 250 nm rods, the measured N_p was moderately (30%) higher than expected. For all lengths, both the size and the number concentration became less reliable as the concentration dipped below 5×10^8 particles/mL.

We also tested 100-nm long polymer-coated nanorods in DI water. N_p was approximately linear with dilution factor due to the

Table 1
Nanoparticle Tracking Analysis of Gold Nanorods

Length (nm)	N_p (10^9 Particles/mL)		d_h (nm)		
	Expected	Measured	Mean	Mode	Theoretical
35	5	5.18 ± 0.23	58 ± 1	37 ± 1	29.5
	0.5	1.10 ± 0.06	82 ± 3	40 ± 1	
	0.05	0.48 ± 0.07	116 ± 11	95 ± 12	
100	5	ND	ND	ND	49
	0.5	3.09 ± 0.04	54 ± 5	46 ± 1	
	0.05	0.71 ± 0.05	90 ± 2	53 ± 1	
250	5	6.58 ± 0.52	91 ± 1	83 ± 1	85
	0.5	0.81 ± 0.04	109 ± 1	99 ± 7	
	0.05	0.13 ± 0.02	112 ± 9	109 ± 17	
100 (polymer)	5	2.00 ± 0.14	66 ± 3	47 ± 1	40
	0.5	0.28 ± 0.03	70 ± 12	45 ± 1	
	0.05	0.04 ± 0.01	94 ± 19	66 ± 19	

Comparison of expected and measured number concentration and hydrodynamic size of gold nanorods of lengths of 35, 100, and 250 nm in 0.5 mm CTAB or 100 nm length coated with NanoPartz positive polymer. The measured mean and mode were compared with the theoretical hydrodynamic diameter d_h. All measurements are the average and standard deviation of 3 independent replicates. ND = not determined, because the particle concentration exceeded maximum that could be tracked accurately.

absence of background scattering contributions. However, N_p was about half that expected based on the manufacturer's reported concentration, with a slightly larger d_h of ~45 nm compared with the expected value of 40 nm. These results are consistent with formation of side-by-side dimers.

We then tested the ability of NTA to track polydisperse solutions of gold nanorods. Mixtures of rods of 35 and 250 nm lengths were prepared (in 0.5 mM CTAB) at 1:1 or 10:1 (35 nm:250 nm) ratios with a total expected particle concentration of 4×10^9 particles/mL and analyzed with NTA (Fig. 2). At a 1:1 ratio, we measured a size and particle concentration of $d_h = 86$ nm (mode) and $N_p = 2.1 \times 10^9$ particles/mL, respectively. These data are consistent with detection of only the 250 nm length rods (theoretical $d_h = 85$ nm, calculated $N_p = 2 \times 10^9$ particles/mL). The 35-nm long rods were completely absent in the measured size distribution. At a ratio of 10:1, a bimodal distribution was obtained, with 2 populations centered near d_h ~45 nm ($N_p = 8 \times 10^7$ particles/mL) and ~105 nm ($N_p = 3.7 \times 10^8$ particles/mL), compared with theoretical expectations of $d_h = 29.5$ nm ($N_p = 3.6 \times 10^9$ particles/mL) and 85 nm ($N_p = 3.6 \times 10^8$ particles/mL), or to experimentally determined values of $d_h = 37$ nm or 83 nm, respectively, for monodisperse solutions of these rods (Table 1). These results are in good agreement with the expected concentration of 250 nm rods, but the measured concentration of 35 nm rods is 45-fold lower than expected. Most likely, this effect is a result of masking of the weakly scattering 35 nm rods by the strongly scattering 250 nm rods. In support of this conclusion, at a number ratio of 1:1, it was necessary to decrease the camera level to 7 due to the strong scattering of the 250 nm rods; increasing the camera to 10 or 13 did not significantly improve detection of the shorter rods (not shown). These results are consistent with other reports on polydisperse mixtures of spherical particles.[15,32]

Taken together, our results support that NTA is able to track the number concentration and hydrodynamic diameter of monodisperse rod-shaped particles in this size range with reasonable accuracy. Although the NanoSight manufacturer's recommended linear range is 10^7-10^9 particles/mL, we found the lower end of this range to yield unreliable particle counts, consistent with reports by others.[33] The best practice is to maintain particle number concentrations between 10^8-5×10^9 particles/mL and to carefully account for any contributions from contaminants in the solution. Given those conditions, one can expect number concentrations to match expected within a factor of 2 or better, and hydrodynamic size to be accurate within 2%-20%, with better accuracy for larger particles. NTA is less accurate at tracking polydisperse mixtures of rods; in particular, the technique greatly underestimates the number concentration of smaller rods when in the presence of larger rods.

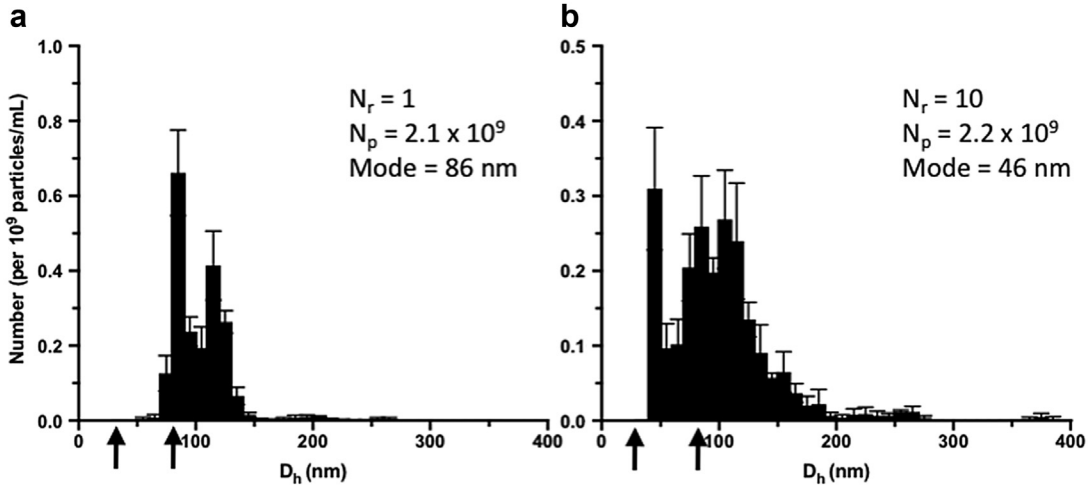

Figure 2. Polydisperse mixtures of 35 nm and 250 nm gold nanorods at number ratios, N_r, of (a) 1:1 and (b) 10:1 for a total particle concentration, N_p, of 4×10^9 particles/mL in 0.5 mM CTAB. Black arrows correspond to the theoretical hydrodynamic diameter for the 35 and 250 nm lengths. (a) For the number ratio, N_r, of 1:1, a camera level of 7 was used with a measured number concentration and mode of 2.1×10^9 particles/mL and 86 nm, respectively. (b) For the number ratio of 10:1, a camera level of 13 was used with a measured number concentration and mode of 2.2×10^9 particles/mL and 46 nm, respectively.

Myosin as a Model of Rod-Like Proteins

Next, we chose the rod-like protein skeletal muscle myosin as a further test of NTA. At high salt concentration (>0.3 M), myosin is an elongated protein containing a long rod-like tail 160 nm long and 2 nm in diameter, with 2 compact globular heads. Myosin was chosen because its rod-like morphology and its length are similar to that of the gold nanorods, and its length and diameter are reminiscent of protofibrils.[34] For a rod-like particle of $L = 160$ nm and $d = 2$ nm, the theoretical d_h equals 34 nm (from Eqs. 2 and 3); researchers have reported experimental values of d_h = 30-35 nm.bib3535,35,36,37 Because myosin is prone to aggregation, the commercially sourced protein was ultracentrifuged before use.

A stock myosin solution was prepared at 0.338 mg/mL in 0.6M KCl, then sequential 10× dilutions were prepared and tested until a suitable particle concentration range for NTA measurements (~10^8 to 10^9 particles/mL) was reached (Fig. 3). Based on the stock solution concentration, myosin molecular weight, and the 100-fold or 1000-fold dilution, we calculated an expected $N_p = 4 \times 10^{12}$ (Fig. 3a) or 4×10^{11} (Fig. 3b), compared with measured values of 2×10^9 or 2×10^8, respectively. In other words, the particle count was only 0.05% of that expected. No particles of the expected hydrodynamic diameter of myosin (~34 nm) were detected. Rather, particles in a broad size range with d_h from 50-150 nm were observed. Buffer alone was dark (data not shown), indicating that the detected particles are not background contaminants. Direct visualization of the myosin sample by TEM confirmed the presence of globule-like protein aggregates in a size range consistent with NTA (Supporting Information Fig. 3). For a control, we also collected NTA data on immunoglobulin M (IgM), an oblate ellipsoid with d_h of 19-28 nm.[35,36] The measured sample was indistinguishable from buffer alone, showing that the aggregates are specific to the myosin preparation and not generally a feature of protein solutions.

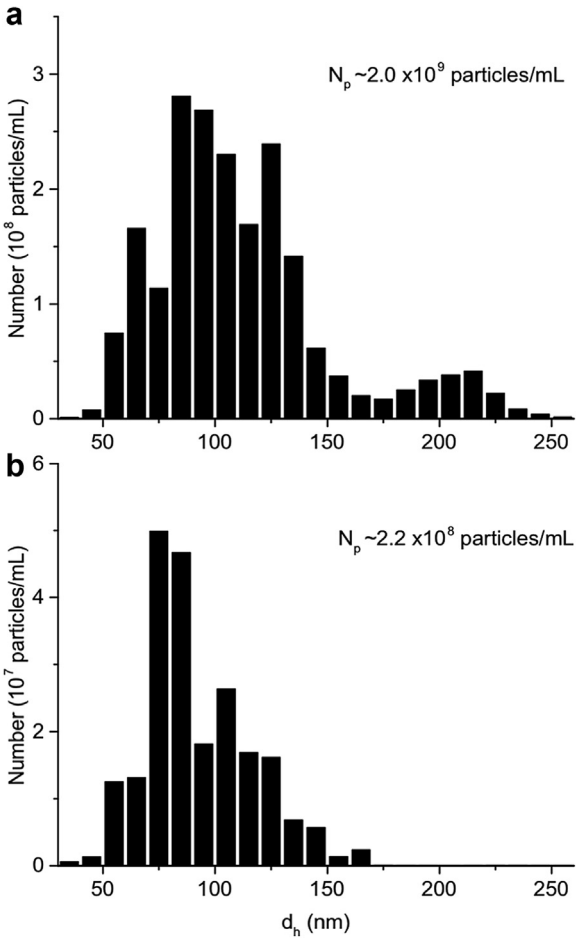

Figure 3. Size distribution (d_h) of detected myosin particles and their number concentration measured by NTA. Myosin from a stock concentration of 0.338 mg/mL was serially diluted (a) 100-fold and (b) 1000-fold. The total number of particles, N_p, detected was ~2×10^9 and 2.2×10^8 for the 100-fold and 1000-fold dilutions, respectively.

NTA yields a number-weighted size distribution. To obtain a mass-based size distribution, a relationship between the molecular weight M and d_h is required. Because the aggregates observed by TEM were globular, we selected 5 large globular proteins with well-established M (g/mol) and d_h (nm): bovine serum albumin, M = 67,000, $d_h = 6.7$ nm; transferrin, $M = 76{,}000$, $d_h = 7.44$ nm; IgG, M = 150,000, $d_h = 10.6$ nm; thyroglobulin, $M = 670{,}000$, $d_h = 17.16$ nm, and $a_2$macroglobulin, $M = 725{,}000$, $d_h = 18.44$ nm.[37-39] These values were regressed to find the relationship:

$$M = 600 d_h^{2.45} \tag{4}$$

We applied Equation 4 to each bin in the NTA distribution (Supporting Information Fig. 3b) and calculated the mass concentration $c = c = N_A^{-1} \sum N_i M_i$, where N_i is the number concentration of particles in bin i (particles/mL) and M_i is the molecular weight for particles of the average size d_{hi} in bin i. This yielded an estimate of $c = 0.000016$ mg/mL. Accounting for the 1000-fold dilution, the mass concentration of aggregates in the undiluted myosin stock solution is 0.016 mg/mL, or 4.7 mass% of the total protein. These results demonstrate a method by which NTA can be used to quantify the percent aggregates in a protein solution.

Given the fact that by NTA we detected only protein aggregates in a preparation that should contain myosin monomers, we analyzed the same myosin sample by SLS (Supporting Information Fig. 4). M_w and R_g, determined by least-squares fit of the data to Equation 1, were 503,000 ± 21,000 g/mol and 51 ± 3 nm, respectively, close to literature values of 500,000-520,000 g/mol and 46 nm[40-42] and consistent with calculated R_g of 46 nm for a thin rigid rod of 160 nm length. Thus, by SLS, the myosin monomer is detected, and there is no strong evidence of aggregates, in complete contrast to NTA data. Finally, the myosin solution was characterized by DLS. The intensity-averaged distribution ($G(\Gamma_i)$) is shown in Figure 4a. A bimodal size distribution was observed, with the 2 peaks centered at 25-30 nm and ~110 nm. The size of the first peak is consistent with myosin monomer.[41,43,44] The second peak corresponds to the large particles detected by NTA and observed under TEM. Taken together, these results demonstrate the remarkable degree to which these 3 light scattering techniques differ with respect to their sensitivity to proteins versus aggregates in a polydisperse mixture. In SLS, myosin monomers dominate the scattering signal and aggregates are essentially absent; NTA is sensitive to very low concentrations of aggregates (NTA measurements were taken at 1000-fold dilution compared with SLS and DLS) but detects no monomer, while DLS spans between the other techniques.

For a quantitative comparison of the protein aggregate population detected by both DLS and NTA, we converted the intensity-averaged distribution obtained by DLS to a mass- and number-average distribution. We found N_i for each bin i by simultaneous solution of i equations of the form:

$$G(\Gamma_i) = \frac{N_i M_i^2}{\sum N_i M_i^2} \tag{5}$$

where i is the total number of bins in the distribution, $G(\Gamma_i)$ is the intensity-weighted distribution determined from CONTIN analysis of the autocorrelation function, and M_i is the molecular weight of

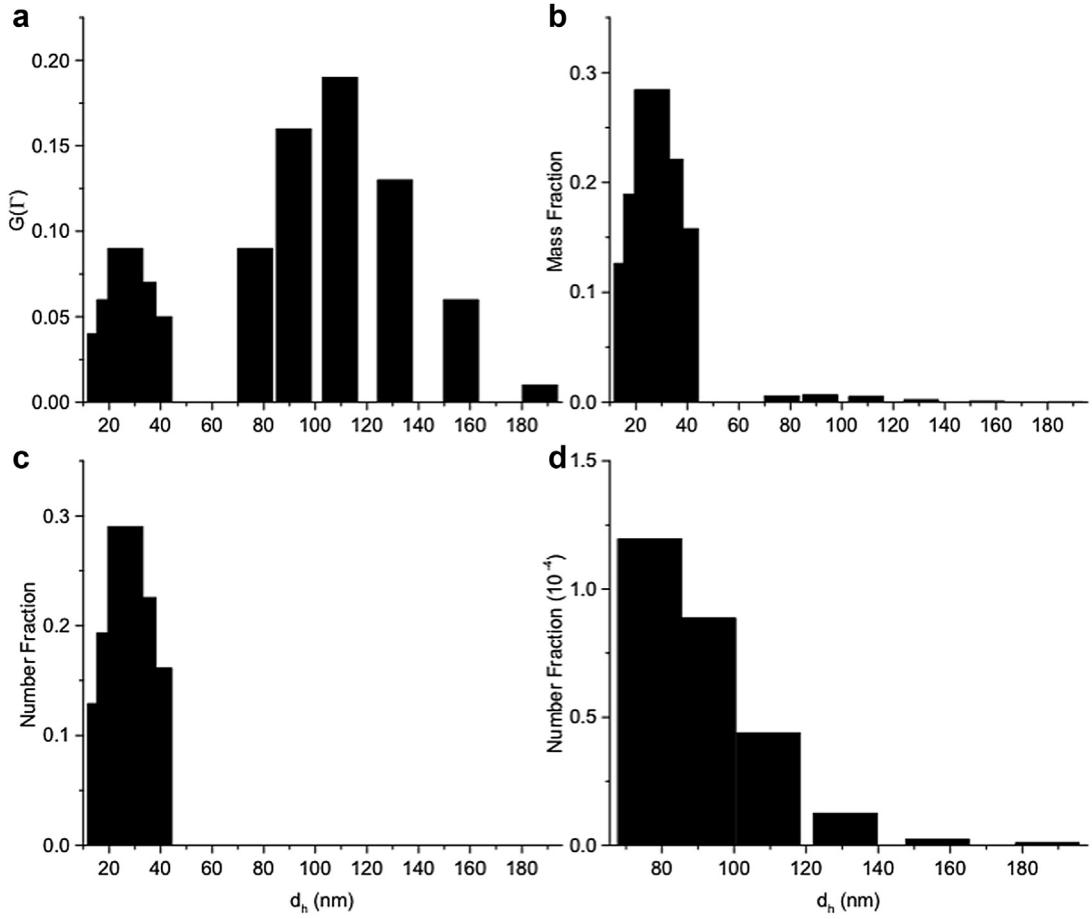

Figure 4. Dynamic light scattering analysis of myosin. (a) Intensity-weighted hydrodynamic diameter distribution determined by CONTIN analysis of the autocorrelation function. (b) Mass-weighted distribution, calculated from the intensity-weighted distribution and Equation 4. (c) Number-weighted size distribution. (d) Close-up of size distribution from 70-200 nm.

the particles in bin i (assumed to be that of myosin monomer, M_i =,503,000, in the first peak and calculated from d_{hi} using Equation 4 for the bins in the second peak), subject to the constraint that $N_A^{-1}\sum N_i M_i = 0.338$ mg/mL. The mass fraction $m_i = N_i M_i / \sum N_i M_i$ and number fraction $n_i = N_i / \sum N_i$ attributed to each bin is then calculated. Results from this analysis are plotted in Figures 4b-4d. The mass percentage of myosin that is aggregated was estimated at 2% from DLS compared with 4.7% from NTA. The particle size distributions of the aggregates obtained from DLS are quite comparable to those obtained from NTA (Fig. 5).

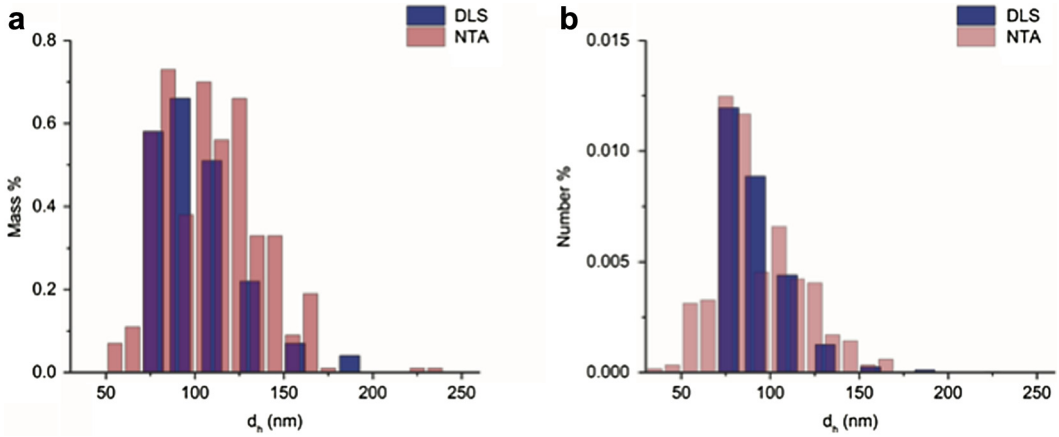

Figure 5. Comparison of the particle size distribution of myosin aggregates detected by NTA (red) and DLS (blue) by mass (a) and number percent (b) for the 1000 fold dilution sample of the myosin stock. The mass and number percentage data measured by DLS was taken from Figures 5b and 5d in the aggregate size range of 75-200 nm, respectively.

Given that d_h of myosin monomer (~34 nm) is within the manufacturer's reported detectable range of NTA (~30 nm for protein) and that we were able to readily detect gold nanorods of similar length, it was surprising that the monomer was completely undetectable by NTA, whereas it was the dominant contributor to SLS and DLS. We hypothesize that this is a result of the anisotropic shape and subsequent low scattering intensity of myosin rods. The scattering intensity per particle, I_P, scales with the molecular weight M, the refractive index increment dn/dc, and the particle scattering factor $P(q)$, as[15]

$$I_P \propto M^2 \left(\frac{dn}{dc}\right)^2 P(q) \tag{6}$$

$P(q)$ of a globular protein of $d_h = 34$ nm modeled as a solid sphere is 0.97.[45] For myosin modeled as a thin rigid rod of length 160 nm,[45] $P(q) = 0.69$. From Equation 4, the molecular weight of a globular protein of $d_h = 34$ nm is $M = 3.3 \times 10^6$ g/mol, or about 6-fold greater than that of myosin. Thus, myosin scatters light poorly relative to a globular protein of similar d_h for 2 reasons:

$$\frac{I_{myosin}}{I_{globular\ protein}} \approx \left(\frac{503,000}{3,300,000}\right)^2 \left(\frac{0.69}{0.97}\right) = 0.0165 \tag{7}$$

These results demonstrate that thin rod-like proteins are much more difficult to detect by NTA compared with globular proteins of similar hydrodynamic size.

Alpha-Synuclein as an Example of Rod-Like Protein Aggregates

Next, we selected aSyn as a model amyloidogenic protein to investigate the potential of NTA for characterization of fibrillar protein aggregates. aSyn is a 14 kDa intrinsically disordered protein that will, under certain conditions, aggregate into thT-positive amyloid fibrils. aSyn aggregates appear as Lewy body deposits in Parkinson's disease and are implicated in disease pathology.[46,47] One of the challenges in characterizing aggregating proteins is that the sample characteristics could change with time during the measurement period, as aggregation proceeds spontaneously. In our hands, aSyn at neutral pH did not aggregate spontaneously if left quiescent; mechanical agitation was needed to initiate aggregation, consistent with other reports.[3,48,49] Another challenge specific to NTA arises on account of the need for dilution of samples to a relatively narrow particle number concentration because dilution could cause dissociation. To address this concern, data were collected from the same sample repeatedly over the course of 10 min, and there was no change in size or number of aggregates. Others have also reported that, once formed, aSyn oligomers and fibrils prepared using similar methods remain stable.[48,50]

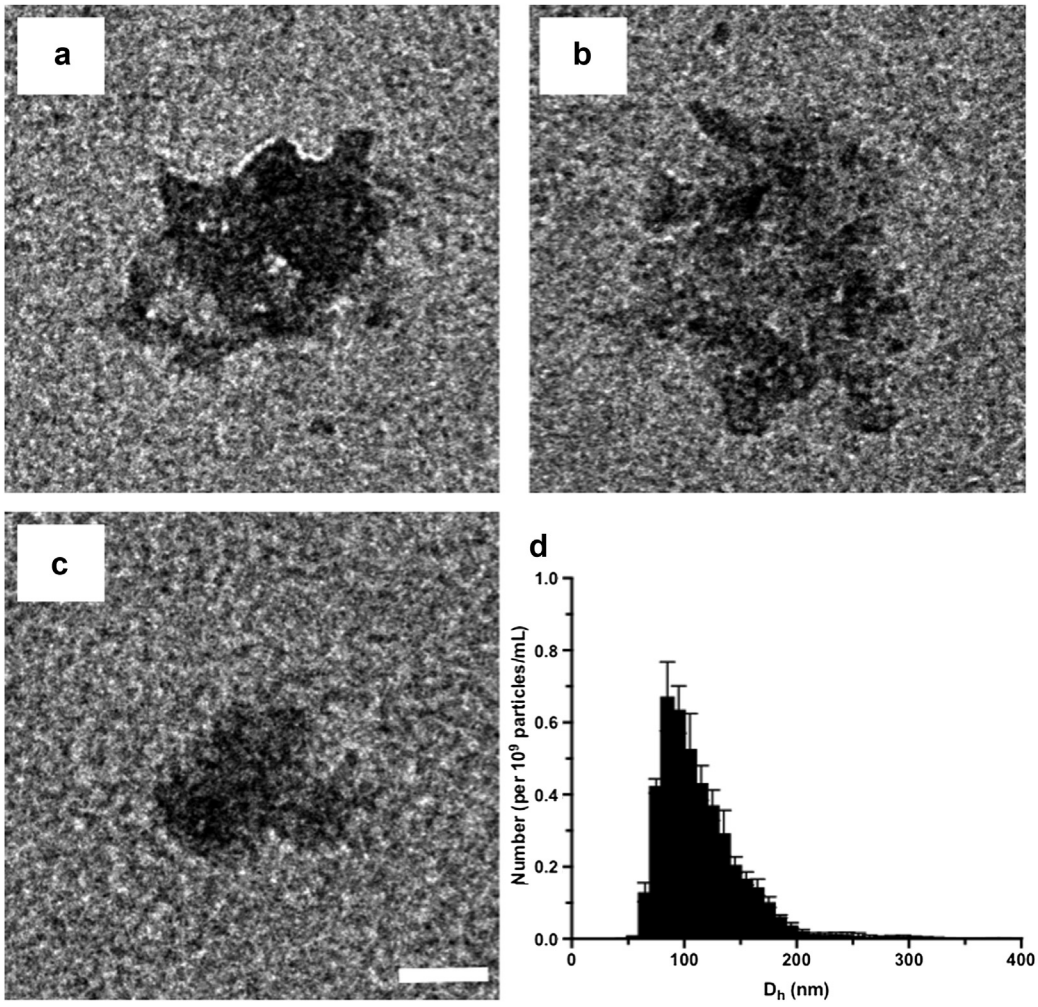

Figure 6. Representative examples of globular aggregates of aSyn observed by TEM at 24 h. (a-c) Aggregates ranged in size from 50-120 nm measured along their longitudinal axis. Scale bar is 50 nm. (d) NTA size distribution of aSyn sample at 24 h exhibited a unimodal distribution. Corrected for dilution, the total particle concentration N_p was 9×10^{11} particles/mL. The mean hydrodynamic diameter (d_h) and mode of particles was 110 and 91 nm, respectively.

Freshly prepared aSyn was ThT-negative (Supporting Information Fig. 5) and exhibited a low number concentration of background scattering particles (7.1×10^7 particles/mL, Supporting Information Fig. 6). This result was expected, as aSyn monomer is below the size detection limit for the Nanosight. No aggregates were observed by TEM (not shown). After 24 h incubation at 37°C in PBS with mechanical agitation, aliquots were removed and evaluated by NTA (Fig. 6d). The sample was diluted until the desired particle concentration range (10^8-10^9 particles/mL) was reached. The particle size distribution was unimodal with a measured mode and mean size of 91 and 111 nm, respectively. Corrected for dilution, the original sample contained $N_p = 9 \times 10^{11}$ particles/mL (compared with 6×10^{16} particles/mL expected if monomers were detected). The sample was ThT-negative (Supporting Information Fig. 5). By TEM, a few aggregates with globule-like morphology were observed (Figs. 6a-6c) with diameters typically 50-120 nm across their longitudinal axis, based on measurements of 11 aggregates in 7 different images. Using the same procedure as described for myosin globular aggregates, we estimated that ~9% of the protein mass was aggregated at 24 h.

After 48 h, the sample became ThT-positive (Supporting Information Fig. 5). Protein aggregates imaged by TEM were fibrillar (Fig. 7) and similar in size and appearance to other reports of aSyn fibrils.[51] Many fibrils appeared in clusters in the images, while others were isolated. The dimensions of 104 isolated fibrils were measured across 16 different TEM images. Rod diameters were typically 14-15 nm, while rod lengths were centered around 220 nm. Fibril dimensions were converted to an equivalent d_h using Equations 2 and 3 and the distribution, centered at 71 nm, is plotted (Fig. 7d).

Fibril clustering, as observed by TEM, was confirmed in preliminary NTA measurements, where some very slowly diffusing and strongly scattering particles were observed (not shown). The sample was therefore centrifuged at low speed, which successfully removed these large particle clusters and reduced the number of counted particles by about 30% (Supporting Information Fig. 7). After centrifugation, the sample was analyzed by NTA and by DLS. The size distribution by NTA was broad and asymmetric, with a mode and mean of 122 and 200 nm, respectively, and a long tail (Fig. 8a). Corrected for dilution, we measured $N_p = 2.7 \times 10^{12}$ particles/mL in the original centrifuged sample. Given the broad distribution as well as our results with a mixture of different-sized gold nanorods, this result almost certainly underestimates the actual number of particles. An intensity-averaged size distribution of the same sample was obtained from DLS and converted to a number-averaged distribution using Equation 5, with the relationship between M and d_h calculated using a mass per length of 118.2 kDa/nm for aSyn fibrils of a similar diameter.[51,52] The result is shown in Figure 8b. DLS produced a bimodal distribution with peaks centered at 120 and 570 nm. The number-averaged distribution from NTA is directly compared with that from DLS in Figure 8c. While a very broad distribution is observed in NTA, analysis of DLS produced 2 modes of well-separated sizes, an artifact that is likely attributable to the tendency for the CONTIN algorithm to oversmooth distributions. This result demonstrates an advantage of NTA; because it measures size on a particle-by-particle basis, the technique may be better able to handle very broad distributions than can DLS.

As described in Equation 6, rod-like particles scatter less light than a globular particle of identical d_h, for 2 reasons: first, because

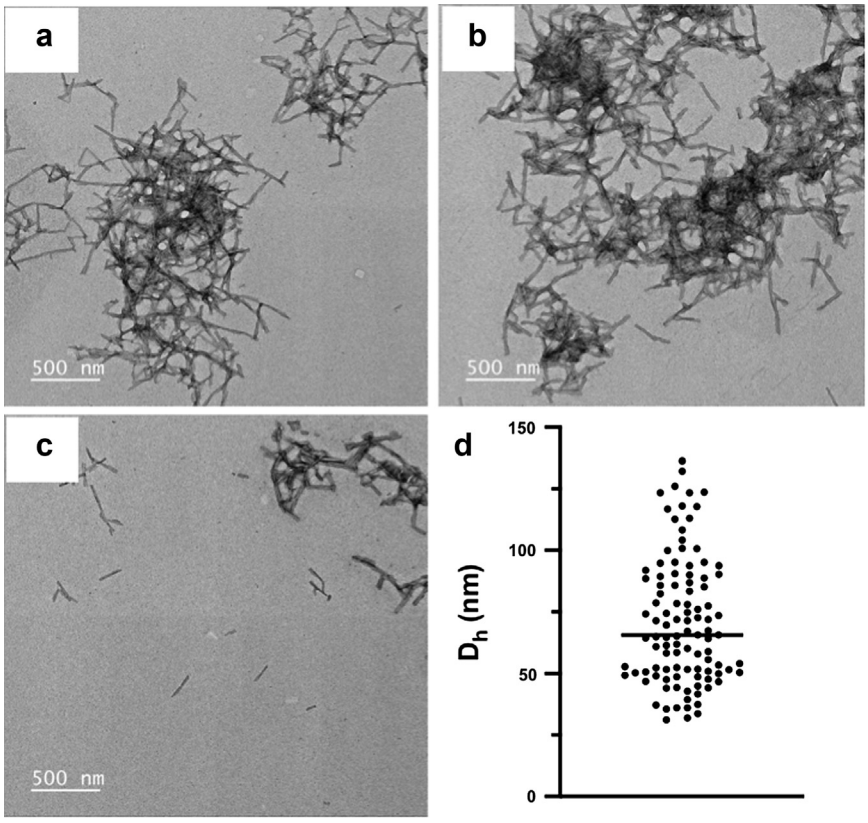

Figure 7. Representative examples of aSyn fibrils visualized by TEM at 48 h. (a-c) Fibrillar aggregates were generally found in clusters. Apart from the clusters, individual rods were often found side-by-side and end-to-end in groups of 2-5 rods. (d) The length and diameter of 104 protofibrils were measured in ImageJ and converted to a hydrodynamic diameter using Equations 2 and 3, with a mean and standard deviation of 70 ± 25 nm.

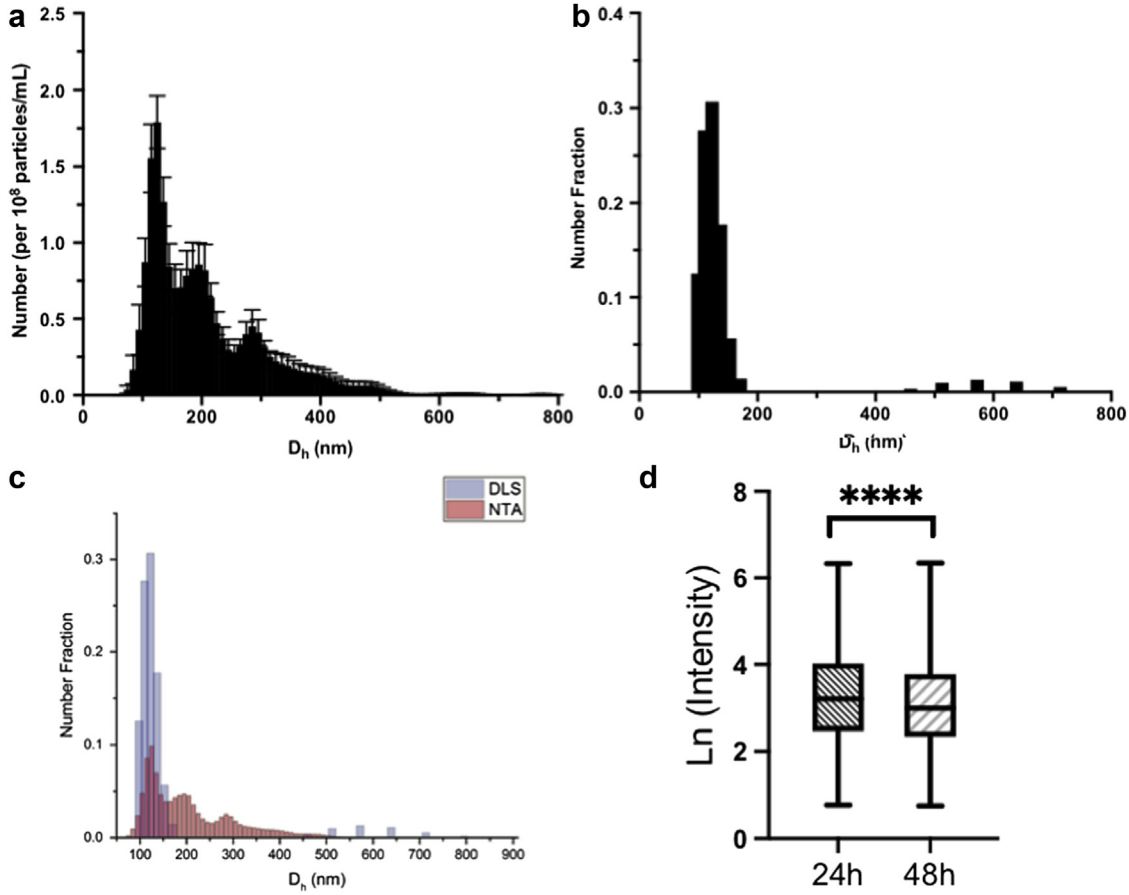

Figure 8. Comparison of the NTA size distribution with the DLS number-weighted distribution for the fibril sample measured at 48 h. (a) NTA showed a broad size distribution with a mean and mode of 200 and 122 nm respectively. Corrected for dilution, the total particle concentration was 2.7×10^{12} particles/mL. (b) DLS scattered intensity distribution was converted to a number-weighted distribution by converting the hydrodynamic diameter in each bin to a length using Equations 2 and 3 and assuming a mass per unit length of 118.2 kDa/nm. Peaks were centered around 120 and 570 nm, respectively. (c) Comparison of the number-weighted size distribution of aggregates detected by NTA (red) and DLS (blue) of aSyn fibrils at 48 h. (d) Box and whiskers analysis of the NTA scattered intensity per particle. A total of 15,932 and 7256 particles were tracked at 24 h and 48 h, respectively. A significant (****$p < 0.0001$) difference in the scattered intensity per particle was observed.

the mass contained in a cylinder is less than that in a solid sphere of equal d_h and specific volume, and second, because $P(q)$ for rods is smaller than for spheres of similar d_h. aSyn fibrillar aggregates have larger cross-sectional area compared with the myosin monomers (e.g., L/d for myosin monomers is $160/2 = 80$, whereas $L/d \sim 10$ for aSyn fibrils of the same length) and therefore do not pose the same difficulty in detection. Still, the scattered intensity of aSyn fibrillar aggregates should be less than that of aSyn globular aggregates of the same d_h. NTA provides particle-by-particle data on not only size but also intensity. Because the incident beam is Gaussian, the scattered intensity from each particle depends on its position in the light field; however, a comparison of the intensity distributions at constant d_h may yield information on changes in particle morphology. To test whether the change from globular to fibrillar morphology could be detected by NTA, we analyzed the scattered intensity per particle using a box and whiskers plot for the samples at 24 h and 48 h, selecting particles in the same hydrodynamic diameter size range of 100-200 nm (Fig. 8d). At 48 h, the scattered intensity per particle was significantly lower ($p < 0.0001$) than that measured at 24 h, consistent with the observed conversion from a globular to an elongated shape.

Summary

NTA has become a useful tool for detecting and measuring spherical or globule-like biological particles such as liposomes or protein aggregates[18-22] but has been used less frequently for anisotropic particles. In this article, we evaluated the ability of NTA to accurately track the size and number concentration of rod-like colloids, protein, and protein aggregates. We first measured the hydrodynamic size and number concentration of gold nanorods, with 10 nm nominal diameter and lengths of 35-250 nm. The best results were obtained at the higher end of the Nanosight manufacturer's reported particle concentration range (10^7-10^9 particles/mL); we recommend 10^8-10^9 particles/mL, consistent with other studies.[28] Gold nanoparticles are prone to aggregation in water[53]; this was readily detected by NTA, and it was necessary to include surfactants or coatings to mitigate aggregation. CTAB, used as a dispersing agent, introduced unwanted contaminants into the buffer, which became an increasingly significant source of error as the gold nanorod concentration was decreased. A polymeric coating on the nanorods eliminated the need for the detergent, thereby eliminating background noise and improving data quality. We observed that the mode of the size distribution was a better measure than the mean, as determined by comparison to theoretical calculations of hydrodynamic diameter. Our results support the conclusion that reasonably reliable simultaneous measures of both number concentration and hydrodynamic size of submicron rod-like particles can be obtained by NTA, provided a sufficient particle concentration is used, and care is taken to eliminate (preferably), or account for, background buffer contributions for monodisperse samples. In mixtures of gold nanorods of different

length, the total number concentration of particles was underestimated, with many of the smaller-sized particles undetected. A similar phenomenon has been observed with polydisperse spherical particles, and this effect is attributed to the strong scattering of larger particles, effectively masking smaller particles in the scattering plane.

We next selected myosin as a protein test case on account of its highly elongated shape ($L/d = 80$) and its hydrodynamic size (d_h ~30-35 nm), within the reported detection range of the instrument.[15,54] Because proteins have a much lower refractive index increment compared with gold,[55,56] we anticipated that detection by NTA might be weaker. However, it was surprising that the number of detected particles was 2000-fold lower than expected, and furthermore, no particles corresponding to myosin monomer were detected. We attributed this result to the fact that elongated proteins have a lower scattering factor $P(q)$ and a lower M/d_h ratio than globular proteins. These combined factors result in a significantly lower scattering intensity for highly elongated proteins compared with globular proteins of the same hydrodynamic size. Myosin is known to be aggregation-prone, and even after ultracentrifugation, a few globular aggregates remained. These aggregates were detected by NTA, but missed by SLS. It is noteworthy that the myosin solution was diluted 100-fold to 1000-fold for NTA compared with the concentration required for conventional ensemble light scattering techniques. Thus, NTA shines at detecting even very low concentrations of protein aggregates. Unique to NTA, the number concentration of aggregates is directly obtained. DLS provided the third view, of a bimodal distribution of myosin monomer and aggregate population. We developed an analysis method that allowed us to compare the size and mass fraction of aggregates determined by DLS with that of NTA. This method required information about the aggregate morphology, which was approximately globular as visualized by TEM.

Finally, we used NTA to examine aggregation of aSyn, a protein that forms amyloid fibrils. Monomeric aSyn is too small to be detected by NTA, and as expected, freshly prepared solutions contained essentially no scattering particles. After 24 h incubation with agitation, the sample remained non-fibrillar, based on the lack of ThT fluorescence. By NTA, some aggregates were detected; TEM confirmed the presence of nonfibrillar aggregates. At 48 h, the protein solution was ThT-positive, and TEM images contained fibrillar aggregates with dimensions typical of aSyn amyloid fibrils. The lengths of isolated fibrils in TEM images were measured and used to calculate a hydrodynamic size distribution; this was compared with NTA-obtained size distributions. The distribution was shifted toward larger aggregates for NTA compared with TEM. This is attributed to 2 factors: first, selecting only fibrils outside of clusters in the TEM images biases the distribution toward shorter fibrils, and second, NTA undercounts smaller aggregates when the solution is polydisperse in size, as demonstrated by the nanorod mixtures. We showed that NTA's unique ability to collect simultaneous particle-by-particle size and intensity data could be used to detect a change in morphology from globular to fibrillar.

With polydisperse protein solutions containing both monomer and aggregates, NTA can provide unique information on particle size distribution, particle number concentration, and changes in particle morphology, in solution and in real time. Drawbacks of the technique include lack of detection of protein aggregates smaller than d_h ~ 30 nm, undercounting of smaller particles in the presence of larger stronger-scattering aggregates, and the need to operate in a very restricted concentration range. Data obtained by NTA are complementary to that accessible with other characterization techniques such as SLS, DLS, and TEM, as we showed in this work. The comprehensive data obtained by adding NTA to the arsenal of the protein scientist will provide more accurate descriptions of the complex mixtures of proteins and protein aggregates that can arise in manufacturing of biopharmaceuticals and can be helpful in developing detailed kinetic models and mechanistic understanding of amyloid fibril growth processes.[48]

Acknowledgment

Funding for this work was provided by the National Science Foundation CBET-1703237 and the William F. Vilas Trust of the University of Wisconsin.

References

1. Scheibel T, Bloom J, Lindquist SL. The elongation of yeast prion fibers involves separable steps of association and conversion. *Proc Natl Acad Sci U S A*. 2004;101(8):2287-2292.
2. Pallitto MM, Murphy RM. A mathematical model of the kinetics of beta-amyloid fibril growth from the denatured state. *Biophys J*. 2001;81(3):1805-1822.
3. Buell AK, Galvagnion C, Gaspar R, et al. Solution conditions determine the relative importance of nucleation and growth processes in -synuclein aggregation. *Proc Natl Acad Sci U S A*. 2014;111(21):7671-7676.
4. Powers ET, Powers DL. Mechanisms of protein fibril formation: nucleated polymerization with competing off-pathway aggregation. *Biophys J*. 2008;94(2):379-391.
5. Ellisdon AM, Pearce MC, Bottomley SP. Mechanisms of ataxin-3 misfolding and fibril formation: kinetic analysis of a disease-associated polyglutamine protein. *J Mol Biol*. 2007;368(2):595-605.
6. Garai K, Frieden C. Quantitative analysis of the time course of Aβ oligomerization and subsequent growth steps using tetramethylrhodamine-labeled Aβ. *Proc Natl Acad Sci U S A*. 2013;110(9):3321-3326.
7. Crespo R, Villar-Alvarez E, Taboada P, Rocha FA, Damas AM, Martins PM. What can the kinetics of amyloid fibril formation tell about off-pathway aggregation? *J Biol Chem*. 2016;291(4):2018-2032.
8. Landrum E, Wetzel R. Biophysical underpinnings of the repeat length dependence of polyglutamine amyloid formation. *J Biol Chem*. 2014;289(15):10254-10260.
9. Bernacki JP, Murphy RM. Model discrimination and mechanistic interpretation of kinetic data in protein aggregation studies. *Biophys J*. 2009;96(7):2871-2887.
10. Murphy RM, Pallitto MM. Probing the kinetics of beta-amyloid self-association. *J Struct Biol*. 2000;130(2-3):109-122.
11. Adamcik J, Mezzenga R. Study of amyloid fibrils via atomic force microscopy. *Curr Opin Colloid Interface Sci*. 2012;17(6):369-376.
12. Carpenter JF, Randolph TW, Jiskoot W, Crommelin DJA, Middaugh CR, Winter G. Potential inaccurate quantitation and sizing of protein aggregates by size exclusion chromatography: essential need to use orthogonal methods to assure the quality of therapeutic protein products. *J Pharm Sci*. 2010;99(5):2200-2208.
13. Crick SL, Jayaraman M, Frieden C, Wetzel R, Pappu RV. Fluorescence correlation spectroscopy shows that monomeric polyglutamine molecules form collapsed structures in aqueous solutions. *Proc Natl Acad Sci U S A*. 2006;103(45):16764-16769.
14. Crick SL, Ruff KM, Garai K, Frieden C, Pappu RV. Unmasking the roles of N- and C-terminal flanking sequences from exon 1 of huntingtin as modulators of polyglutamine aggregation. *Proc Natl Acad Sci U S A*. 2013;110(50):20075-20080.
15. Yang DT, Lu X, Fan Y, Murphy RM. Evaluation of nanoparticle tracking for characterization of fibrillar protein aggregates. *AIChE J*. 2014;60(4):1236-1244.
16. Filipe V, Hawe A, Jiskoot W. Critical evaluation of nanoparticle tracking analysis (NTA) by NanoSight for the measurement of nanoparticles and protein aggregates. *Pharm Res*. 2010;27(5):796-810.
17. Gallego-Urrea JA, Tuoriniemi J, Hassellöv M. Applications of particle-tracking analysis to the determination of size distributions and concentrations of nanoparticles in environmental, biological and food samples. *TrAC Trends Anal Chem*. 2011;30(3):473-483.
18. Tian X, Nejadnik MR, Baunsgaard D, Henriksen A, Rischel C, Jiskoot W. A comprehensive evaluation of nanoparticle tracking analysis (NanoSight) for characterization of proteinaceous submicron particles. *J Pharm Sci*. 2016;105(11):3366-3375.
19. Sediq AS, van Duijvenvoorde RB, Jiskoot W, Nejadnik MR. No touching! Abrasion of adsorbed protein is the root cause of subvisible particle formation during stirring. *J Pharm Sci*. 2016;105(2):519-529.
20. Bickel F, Herold EM, Signes A, Romeijn S, Jiskoot W, Kiefer H. Reversible NaCl-induced aggregation of a monoclonal antibody at low pH: characterization of aggregates and factors affecting aggregation. *Eur J Pharm Biopharm*. 2016;107:310-320.
21. Filipe V, Kükrer B, Hawe A, Jiskoot W. Transient molten globules and metastable aggregates induced by brief exposure of a monoclonal IgG to low pH. *J Pharm Sci*. 2012;101(7):2327-2339.
22. Chen C, Zhu S, Huang T, Wang S, Yan X. Analytical techniques for single-liposome characterization. *Anal Methods*. 2013;5(9):2150.

23. Casas J, Venkataramasubramani M, Wang Y, Tang L. Replacement of cetyltrimethylammoniumbromide bilayer on gold nanorod by alkanethiol cross-linker for enhanced plasmon resonance sensitivity. *Biosens Bioelectron*. 2013;49:525-530.
24. Trybus KM, Lowey S. Conformational states of smooth muscle myosin. Effects of light chain phosphorylation and ionic strength. *J Biol Chem*. 1984;259(13):8564-8571.
25. Pecora R. Dynamic light scattering measurement of nanometer particles in liquids. *J Nanoprat Res*. 2000;2(2):123-131.
26. Arnold JN, Wormald MR, Suter DM, et al. Human serum IgM glycosylation: identification of glycoforms that can bind to mannan-binding lectin. *J Biol Chem*. 2005;280(32):29080-29087.
27. Glidden M, Muschol M. Characterizing gold nanorods in solution using depolarized dynamic light scattering. *J Phys Chem C*. 2012;116(14):8128-8137.
28. Tirado MM, Martinez CL, Garcia de la Torre J. Comparison of theories for the translational and rotational diffusion coefficients of rodlike macromolecules. *J Chem Phys*. 1984;81:2047-2052.
29. Harris ELV, Angal S, eds. *Protein Purification Applications: A Practical Approach*. Oxford, NY: IRL Press at Oxford University Press; 1990.
30. Neugebauer JM. Detergents: an overview. *Meth Enzymol*. 1990;182:239-253.
31. Patel V, Dharaiya N, Ray D, Aswal VK, Bahadur P. pH controlled size/shape in CTAB micelles with solubilized polar additives: a viscometry, scattering and spectral evaluation. *Colloids Surf A*. 2014;455:67-75.
32. Domingos RF, Baalousha MA, Ju-Nam Y, et al. Characterizing manufactured nanoparticles in the environment: multimethod determination of particle sizes. *Environ Sci Technol*. 2009;43(19):7277-7284.
33. Zhou C, Krueger AB, Barnard JG, Qi W, Carpenter JF. Characterization of Nanoparticle Tracking Analysis for quantification and sizing of submicron particles of therapeutic proteins. *J Pharm Sci*. 2015;104(8):2441-2450.
34. Ruggeri FS, Benedetti F, Knowles TPJ, Lashuel HA, Sekatskii S, Dietler G. Identification and nanomechanical characterization of the fundamental single-strand protofilaments of amyloid α-synuclein fibrils. *Proc Natl Acad Sci U S A*. 2018;115(28):7230-7235.
35. Akhouri RR, Goel S, Furusho H, Skoglund U, Wahlgren M. Architecture of human IgM in complex with P. Falciparum erythrocyte membrane protein 1. *Cell Rep*. 2016;14(4):723-736.
36. Radomsky M. Macromolecules released from polymers: diffusion into unstirred fluids. *Biomaterials*. 1990;11(9):619-624.
37. Yarmush DM, Murphy RM, Colton CK, Fisch M, Yarmush ML. Quasi-elastic light scattering of antigen-antibody complexes. *Mol Immunol*. 1988;25(1):17-32.
38. Separation of proteins mixture in hollow fiber flow field-flow fractionation. *Bull Korean Chem Soc*. 2003;24(9):1339-1344.
39. Armstrong JK, Wenby RB, Meiselman HJ, Fisher TC. The hydrodynamic radii of macromolecules and their effect on red blood cell aggregation. *Biophys J*. 2004;87(6):4259-4270.
40. Gellert MF, Englander SW. The molecular weight of rabbit myosin A by light scattering. *Biochemistry*. 1963;2(1):39-42.
41. Herbert TJ, Carlson FD. Spectroscopic study of the self-association of myosin. *Biopolymers*. 1971;10(11):2231-2252.
42. Lowey S, Holtzer A. The aggregation of myosin. *J Am Chem Soc*. 1959;81(6):1378-1383.
43. Wu X, Blank PS, Carlson FD. A quasi-elastic light scattering study of smooth muscle myosin in the presence of ATP. *Biophys J*. 1992;63(1):169-179.
44. Trybus KM, Huiatt TW, Lowey S. A bent monomeric conformation of myosin from smooth muscle. *Proc Natl Acad Sci U S A*. 1982;79(20):6151-6155.
45. *Misbehaving Proteins*. New York, NY: Springer New York; 2006.
46. Spillantini MG, Schmidt ML, Lee VM-Y, Trojanowski JQ, Jakes R, Goedert M. α-Synuclein in Lewy bodies. *Nature*. 1997;388(6645):839-840.
47. Spillantini MG, Crowther RA, Jakes R, Hasegawa M, Goedert M. α-Synuclein in filamentous inclusions of Lewy bodies from Parkinson's disease and dementia with Lewy bodies. *Proc Natl Acad Sci U S A*. 1998;95(11):6469-6473.
48. Iljina M, Garcia GA, Horrocks MH, et al. Kinetic model of the aggregation of alpha-synuclein provides insights into prion-like spreading. *Proc Natl Acad Sci U S A*. 2016;113(9):E1206-E1215.
49. Flynn JD, McGlinchey RP, Walker RL, Lee JC. Structural features of α-synuclein amyloid fibrils revealed by Raman spectroscopy. *J Biol Chem*. 2018;293(3):767-776.
50. Cremades N, Cohen SIA, Deas E, et al. Direct observation of the interconversion of normal and toxic forms of α-Synuclein. *Cell*. 2012;149(5):1048-1059.
51. Qin Z, Hu D, Han S, Hong D-P, Fink AL. Role of different regions of α-Synuclein in the assembly of fibrils. *Biochemistry*. 2007;46(46):13322-13330.
52. Dearborn AD, Wall JS, Cheng N, et al. α-Synuclein amyloid fibrils with two entwined, asymmetrically associated protofibrils. *J Biol Chem*. 2016;291(5):2310-2318.
53. Ma Z, Tian L, Wang T, Wang C. Optical DNA detection based on gold nanorods aggregation. *Anal Chim Acta*. 2010;673(2):179-184.
54. Lu X, Murphy RM. Nanoparticle Tracking for protein aggregation research. In: Nilsson BL, Doran TM, eds. *Peptide Self-Assembly*. Vol. 1777. New York, NY: Springer New York; 2018:145-158.
55. Zhao H, Brown PH, Schuck P. On the distribution of protein refractive index increments. *Biophys J*. 2011;100(9):2309-2317.
56. Rakić AD, Djurišić AB, Elazar JM, Majewski ML. Optical properties of metallic films for vertical-cavity optoelectronic devices. *Appl Opt*. 1998;37(22):5271.